Astronomy & Astrophysics

The WISSH quasars project

VIII. Outflows and metals in the circum-galactic medium around the hyper-luminous *z* ~ 3.6 quasar J1538+08[★,★★]

A. Travascio[1,2,3], L. Zappacosta[1], S. Cantalupo[4], E. Piconcelli[1], F. Arrigoni Battaia[5,6], M. Ginolfi[7], M. Bischetti[1], G. Vietri[8], A. Bongiorno[1], V. D'Odorico[9,10], F. Duras[11], C. Feruglio[9], C. Vignali[12,13], and F. Fiore[9]

[1] INAF-Osservatorio Astronomico di Roma, Via Frascati 33, 00078 Monteporzio Catone, Italy
e-mail: andrea.travascio@inaf.it
[2] Department of Physics, University of Rome "Tor Vergata", Via della Ricerca Scientifica 1, 00133 Rome, Italy
[3] Università degli Studi di Roma "Sapienza", Piazzale Aldo Moro 5, 00185 Roma, Italy
[4] Department of Physics, ETH Zurich, Wolfgang-Pauli-Strasse 27, 8093 Zurich, Switzerland
[5] European Southern Observatory, Karl-Schwarzschild-Str. 2, 85748 Garching bei Munchen, Germany
[6] Max-Planck-Institut fur Astrophysik, Karl-Schwarzschild-Str 1, 85748 Garching, Germany
[7] Observatoire de Genève, Université de Genève, 51 Ch. des Maillettes, 1290 Versoix, Switzerland
[8] INAF, Istituto di Astrofisica Spaziale e Fisica Cosmica – Milano, Via A. Corti 12, 20133 Milano, Italy
[9] INAF Osservatorio Astronomico di Trieste, Via G.B. Tiepolo, 11, Trieste 34143, Italy
[10] Scuola Normale Superiore, Piazza dei Cavalieri 7, 56126 Pisa, Italy
[11] Dipartimento di Matematica e Fisica, Università Roma Tre, Via della Vasca Navale 84, 00146 Roma, Italy
[12] Dipartimento di Fisica e Astronomia, Università di Bologna, Via Piero Gobetti 93/2, 40129 Bologna, Italy
[13] INAF-Osservatorio di Astrofisica e Scienza dello Spazio di Bologna, Via Piero Gobetti 93/3, 40129 Bologna, Italy

ABSTRACT

Context. In recent years, Lyα nebulae have been routinely detected around high redshift, radio-quiet quasars thanks to the advent of the highly sensitive integral field spectrographs. Constraining the physical properties of the Lyα nebulae is crucial for a full understanding of the circum-galactic medium (CGM). The CGM acts both as a repository for intergalactic and galactic baryons as well as a venue of feeding and feedback processes. The most luminous quasars are privileged test-beds to study these processes, given their large ionising fluxes and dense CGM environments in which they are expected to be embedded.
Aims. We aim to characterise the rest-frame ultraviolet (UV) emission lines in the CGM around a hyper-luminous, broad emission line, radio-quiet quasar at $z \sim 3.6$, which exhibits powerful outflows at both nuclear and host galaxy scales.
Methods. We analyse VLT/MUSE observations of the quasar J1538+08 ($L_{\rm bol} = 6 \times 10^{47}\,{\rm erg\,s^{-1}}$), and we performed a search for extended UV emission lines to characterise its morphology, emissivity, kinematics, and metal content.
Results. We report the discovery of a very luminous ($\sim 2 \times 10^{44}\,{\rm erg\,s^{-1}}$), giant Ly$\alpha$ nebula and a likely associated extended (75 kpc) CIV nebula. The Lyα nebula emission exhibits moderate blueshift ($\sim 440\,{\rm km\,s^{-1}}$) compared to the quasar systemic redshift and a large average velocity dispersion ($\bar{\sigma}_{\rm v} \sim 700\,{\rm km\,s^{-1}}$) across the nebula, while the CIV nebula shows average velocity dispersion of $\bar{\sigma}_{\rm v} \sim 350\,{\rm km\,s^{-1}}$. The Ly$\alpha$ line profile exhibits a significant asymmetry towards negative velocity values at $20-30$ kpc south of the quasar and is well parametrised by the following two Gaussian components: a narrow ($\sigma \sim 470\,{\rm km\,s^{-1}}$) systemic one plus a broad ($\sigma \sim 1200\,{\rm km\,s^{-1}}$), blueshifted ($\sim 1500\,{\rm km\,s^{-1}}$) one.
Conclusions. Our analysis of the MUSE observation of J1538+08 reveals metal-enriched CGM around this hyper-luminous quasar. Furthermore, our detection of blueshifted emission in the emission profile of the Lyα nebula suggests that powerful nuclear outflows can propagate through the CGM over tens of kiloparsecs.

Key words. galaxies: active – intergalactic medium – quasars: emission lines – quasars: individual: SDSS 153830.55+085517.0

1. Introduction

In the past few decades, the investigation of extended (tens of kiloparsec-scales) Lyα-emitting nebulae surrounding active galaxies have become more and more intense (see Cantalupo et al. 2017 and references therein). These are a promising

repository for the census of baryonic matter and metals, and they are a privileged environment to study the feeding and feedback processes. The first circum-galactic medium (CGM) emission nebulae detected in Lyα (Lyα-CEN hereafter) were mostly observed around high redshift radio galaxies with sizes exceeding 100 kpc, through narrow-band (NB) imaging and slit spectroscopy (e.g. Heckman et al. 1991; van Ojik et al. 1997; Villar-Martín et al. 2006, 2007a; Humphrey et al. 2007, 2013). Only a minor fraction ($\sim 10\%$) of them were reported around radio-quiet quasars (RQQs; e.g. Weidinger et al. 2005; Christensen et al. 2006; Arrigoni Battaia et al. 2016). In rare cases, RQQs have been found lying in overdense active galactic

---

nuclei (AGN) environments and embedded in enormous Lyα nebulae (ELANe) with projected sizes exceeding $\sim$200 kpc and surface brightnesses (SB) $> 10^{-17}$ erg s^{-1} cm^{-2} arcsec^{-2} for hundreds of kiloparsecs (Cantalupo et al. 2014; Hennawi et al. 2015; Cai et al. 2017a). Recent sensitive integral field spectrographs, such as VLT/MUSE (Multi Unit Spectroscopic Explorer; Bacon et al. 2010) and Keck/KCWI (Keck Cosmic Web Imager), have recently allowed for the detection of extended Lyα emission around $z = 2-5$ quasars at a depth that has never been explored before and provided a 3D view of Lyα-CEN. Borisova et al. (2016, hereafter B16) and Arrigoni Battaia et al. (2019, hereafter AB19) performed MUSE surveys of optically-bright RQQs at $3 < z < 4$. Also, Cai et al. (2019) used the KCWI to study the CGM surrounding RQQs at $z \approx 2$ and they report detection rates of nearly 100% for Lyα-CEN.

Detailed morphological and kinematic studies of Lyα-CEN reveal that they have large ($\sim$100 kpc diameter) and mostly symmetrical structures with the bulk of their emission concentrated within tens of kiloparsecs (B16; AB19; Ginolfi et al. 2018; Lusso et al. 2019). Their average SB profiles have been parameterised with exponential (AB19) or power-law (B16) profiles with no clear dependence on radio-loudness (AB19). Although with a few exceptions (e.g. Weidinger et al. 2004, 2005; Cai et al. 2017b; Arrigoni Battaia et al. 2018), Lyα-CEN do not show any clear kinematic pattern (e.g. when ascribed to ordered gas rotation or inflows and outflows) and they exhibit velocity dispersions of $\sigma_v \lesssim 400$ km s^{-1}. The latter are consistent with the expected kinematics of their dark matter halo gravitational potential. However, higher σ_v values have been reported for CEN around some RQQs and radio-loud sources (B16; Ginolfi et al. 2018). For the latter, the high σ_v is likely due to the jets mechanical interaction with the Lyα-CEN (van Ojik et al. 1997; Villar-Martín et al. 2006; Silva et al. 2018).

To date, at least three mechanisms have been proposed to explain extended Lyα emission of cold ($T \sim 10^4$ K) gas. The main one is fluorescence, which was predicted for the first time by Hogan & Weymann (1987), whereby the gas emits Lyα photons by recombination when it is photoionised by one or more UV sources (Cantalupo et al. 2005). The second is associated with AGN Lyα photons, which can be resonantly scattered by the neutral hydrogen clouds (Møller & Warren 1998; Cantalupo et al. 2005). Finally, shocks triggered by galactic outflows can power Lyα emission (Taniguchi & Shioya 2000; Arrigoni Battaia et al. 2015a). The contribution of all these mechanisms is expected to be large in the CGM surrounding hyperluminous ($L_{bol} \gtrsim 10^{47}$ erg s^{-1}) quasars. Indeed, the latter are the most luminous UV emitters (Duras et al. 2017) and sit on large potential wells, which likely suggest the presence of relatively high-density CGM and significant over-density of companions (Bischetti et al. 2018). Furthermore, luminous quasars are also predicted and observed to launch the most powerful winds out to host-galaxy scales (Faucher-Giguère & Quataert 2012; Fiore et al. 2017; Menci et al. 2019. Hence, we can reasonably expect them to affect the kinematics of the CGM and its metal content.

In this paper we report VLT/MUSE observations of SDSS J153830.55+085517.0 (hereafter J1538+08), a hyperluminous ($L_{bol} \approx 6 \times 10^{47}$ erg s^{-1}) quasar at $z_{QSO} = 3.567^{+0.003}_{-0.002}$ (based on Hβ; Vietri et al. 2018). This source belongs to the WISE/SDSS-selected hyper-luminous quasar (WISSH) sample (Bischetti et al. 2017), that is, the optically and mid-infrared selected most luminous quasars at $z = 2-4$. The WISSH quasars are characterised by pervasive powerful winds from nuclear (Vietri et al. 2018; Bruni et al. 2019) out to kiloparsec scales

(Bischetti et al. 2017) and, hence, they are ideal laboratories for a detailed study of the kinematics and metal content at CGM scales.

The paper is organised as follows: Sects. 2 and 3 describe the reduction of the MUSE data and the methodology for CEN detection, respectively. Section 4 presents the results of our analysis along with the physical properties of the CEN revealed around J1538+08. Section 5 is devoted to the discussion of the Lyα-CEN properties, the presence of metals (i.e. CIV-CEN), and the evidence of an outflow in the CGM traced by the blueshifted Lyα emission. Finally, Sect. 6 reports our conclusions. Throughout the paper we adopt a cosmology with $\Omega_\Lambda = 0.68$ and $H_0 = 67.4$ km s^{-1} Mpc^{-1} (Planck Collaboration VI 2018), for which 1 arcsec corresponds to $\sim$7.4 kpc at the quasar redshift. All of the errors are quoted at 1σ significance and all flux-weighted quantities were computed for regions with an $S/N \geq 3$, unless stated otherwise.

2. Data reduction

J1538+08 was observed with MUSE on July 26, 2017, as part of the ESO programme ID 099.A-0316(A) (PI F. Fiore). The observation consists of four exposures of 1020 s each, for a total integration time of one hour and eight minutes. Each exposure was rotated by 90° with the addition of a small dithering. The average seeing was $\approx$0.9 arcsec. The data reduction was performed by using the ESO MUSE pipeline (EsoRex v. 3.12.3; Weilbacher et al. 2014) and the code CubExtractor (CubEx v. 1.8; see Cantalupo et al. 2019). We followed a procedure similar to the one reported in B16, which is described in more detail by Cantalupo et al. (2019). We briefly summarise the main steps as follows. For each exposure, we applied bias subtraction and corrected for flat-fielding, twilight, and illumination, using the standard ESO MUSE pipeline. Finally, we applied a wavelength, geometry, and astrometric calibration.

Firstly, we used CubeFix (a tool from the CubExtractor Package) to apply a more accurate flat-fielding correction in each datacube by using the continuum and the emission lines of the sky as calibrators. This procedure consists in deriving the correction factors to be applied to each integral field unit (IFU) and its elements to have coherent values of the sky on the whole field of view (FOV). This allowed us to perform a wavelength and flux dependent correction. The continuum of the sources need to be iteratively masked to minimise the self-calibration errors.

Secondly, we performed a correction of the sky line spread function with the CubeSharp procedure, which adopts a flux-conserving sky-subtraction method (see Cantalupo et al. 2019).

Then, CubEx was used to obtain more refined science datacubes and the associated variances. It is important to note that the standard ESO pipeline can underestimate the propagated variance (Bacon et al. 2017). This variance was therefore propagated during the execution of CubExtractor packages and rescaled by a constant factor to match the empirical spatial variance estimated from the cube at each wavelength layer (see Borisova et al. 2016, for details). The final datacube is a median stack (with 3σ-clipping) of the single datacubes derived from each exposure.

Finally, we notice that during the data reduction with the CubExtractor code, we account for the presence of a saturated bright (Vega magnitude $V \simeq 9.7$) star at the edge of the MUSE FOV contaminating large part of the field in each exposure. In the flat-fielding and sky-subtraction, we indeed masked the stellar emission and the bleed trails up to a distance of 16 arcsec

from the quasar where this contribution starts to become negligible for our purposes (see Appendix A for further details).

3. CEN detection methodology

We performed the identification and extraction of the CEN in the final datacube with the `CubExtractor` package. We first removed the quasar point spread function (PSF) with the `CubePSFSub` task by masking the expected spectral regions that have an extended emission in order to avoid any contamination in the PSF estimation. This recipe estimates the quasar PSF empirically at each wavelength layer from a pseudo-NB image. In our case, each pseudo-NB image was computed with a spectral width of ± 150 pixels, corresponding to $\pm 188\,\text{Å}$. The estimated PSF was rescaled to its flux in each wavelength layer image and then subtracted. The PSF normalisation was derived by assuming that the central pixels, within a region of $1'' \times 1''$, are quasar dominated. Furthermore, we removed the continuum emission of any source within the MUSE FOV by means of a fast median-filtering approach using the `CubeBKGSub` task (see Cantalupo et al. 2019 for further details).

We searched for diffuse emission in the PSF- and continuum-subtracted datacube with the `CubEx` recipe. The latter allowed us to detect and extract extended sources by applying a connected labelling component algorithm. The key input parameters of this algorithm are $N_{\text{min}}^{\text{vox}}$ and S/N_{th}, which define the minimum number of connected voxels and the signal-to-noise ratio (S/N) threshold of the extended emission that is to be searched for, respectively. `CubEx` returns astrometric, photometric, and spectroscopic information on the extended nebular emissions and generates both a three-dimensional mask (3D-mask), which defines the datacube elements (i.e. voxels) belonging to the detected nebula, and a 3D S/N cube. Once the CEN was detected and extracted, the `Cube2Im` task allowed us to create, for the detected CEN, the following three data products by using the voxels of the PSF- and continuum-subtracted datacube defined in the 3D-mask: (i) the SB map, that is, an "optimally extracted image" derived by applying the 3D-mask to the datacube and by collapsing, at each spaxel, the contribution of the nebula voxels above the chosen S/N_{th}; (ii) a map of the velocity distribution obtained as the first moment of the flux distribution; and (iii) a map of σ_{v}, which was derived as the second moment of the flux distribution. All these data products were smoothed with a Gaussian-kernel of $\sigma = 2$ pixels (0.4 arcsec). We computed the S/N map from the pseudo-NB image obtained by collapsing the wavelength range (i.e. the layers) in which the extended emission was detected to have an estimation of the variance distribution of the SB map. Then we associated an S/N value to each pixel, where the noise is the average of the standard deviations derived in several background regions with a size of $1'' \times 1''$. The S/N map was finally smoothed with a Gaussian-kernel of $\sigma = 2$ pixels, in order to be consistent with the smoothing of the maps produced by `Cube2Im`.

4. Results

We searched for CEN around J1538+08 traced by typical CGM UV transitions, such as Lyα $\lambda 1215\,\text{Å}$, NV$\lambda 1240\,\text{Å}$, SiIV$\lambda 1397\,\text{Å}$, CIV$\lambda 1549\,\text{Å}$, HeII$\lambda 1641\,\text{Å}$, and CIII]$\lambda 1909\,\text{Å}$. We detected significant nebular emission in Lyα and CIV. The properties of the detected CEN are described in the following sections.
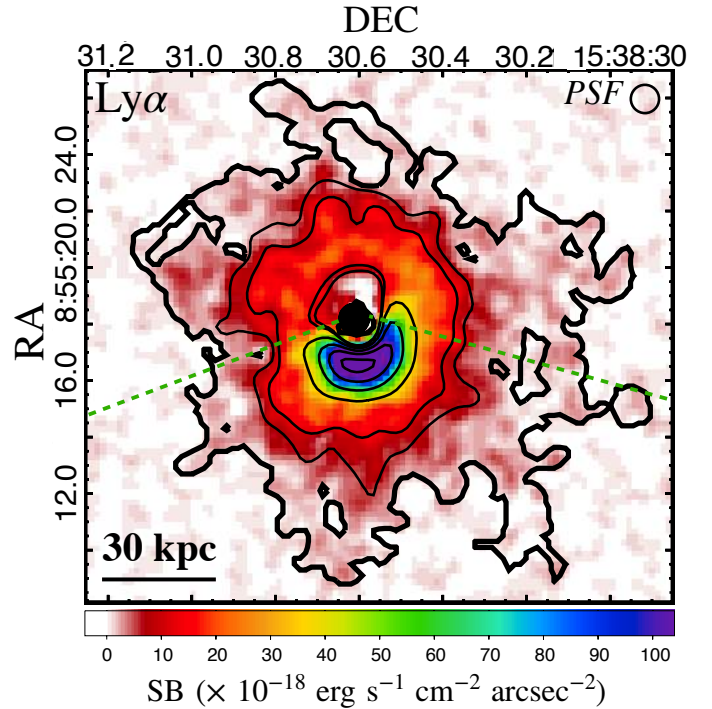
Fig. 1. Optimally extracted SB map of the Lyα-CEN. The quasar position is marked by a black dot. The thick black contour corresponds to the two-dimensional projection of the boundary of the CEN from the 3D-mask. It indicates an SB level of about $10^{-18}\,\text{erg s}^{-1}\,\text{cm}^{-2}\,\text{arcsec}^{-2}$. The thin black contours indicate the S/N levels $3, 5, 15, 25, 35$, and 45 extracted from the S/N map. The wavelength layer at the Lyα profile peak is used to report the background fluctuations in the image. On the top-right corner, the circle indicates the size of the FWHM of the instrument PSF. The green dashed lines delimit two regions of the Lyα-CEN (i.e. north and south from the quasar position) used for the extraction of the radial profile (see Fig. 3). The low-S/N region close to the quasar with SB values around zero could be the result of either random fluctuations or real features of the distribution of the CGM gas emission.

4.1. Lyα nebula

We found a Lyα-CEN consisting of $\sim 55\,000$ connected voxels by using $S/N_{\text{th}} = 2.5$ and $N_{\text{min}}^{\text{vox}} = 10\,000$ pixels. This CEN exhibits a maximum angular extension of ~ 20 arcsec ($\sim 150\,\text{kpc}$). The line emission integrated over the entire CEN spans a maximum wavelength range of $\sim 95\,\text{Å}$ ($\sim 5000\,\text{km s}^{-1}$) and shows a peak measured through a Gaussian fit at $\lambda_{\text{Ly}\alpha}^{\text{CEN}} = (5543.8 \pm 1.8)\,\text{Å}$. This corresponds to a redshift of $z_{\text{CEN}}^{\text{Ly}\alpha} = 3.560 \pm 0.002$.

Figure 1 shows the SB map of the Lyα-CEN. The nebular emission is the region enclosed in the black thick contour, that is, the projected boundary derived from the 3D-mask, which encloses the detected CEN with $S/N > 2.5$. The thin contours indicate the S/N levels derived from the S/N map. This Lyα-CEN exhibits a roughly symmetric shape on large scales suggesting a circular, or mildly elliptical, morphology with marked deviations at small radii. In order to obtain a more quantitative description of its morphology, we computed the flux weighted centroid shift ($d_{\text{CEN}}^{\text{cen}}$), the peak displacement ($d_{\text{CEN}}^{\text{peak}}$), the asymmetry ($\alpha$), and the position angle east of north (ϕ) of the CEN. The first two quantities were measured with respect to the quasar position, while the remaining ones were estimated from the Stokes parameters as in AB19 (see Table 1). We find general

Table 1. Physical properties of the detected CEN.

	Lyα	CIV
$\lambda_{\rm CEN}$ [Å] [a]	5543.8 ± 1.8	7064.7 ± 1.8
$z_{\rm CEN}$ [b]	3.560 ± 0.002	3.559 ± 0.001
Size [kpc] [c]	150	75
Spectral width [Å] [d]	95	42
$d_{\rm CEN}^{\rm peak}$ [kpc] [e]	10.4 ± 3.7 [⋆]	15.1 ± 3.7 [⋆]
$d_{\rm CEN}^{\rm cen}$ [kpc] [f]	5.7 ± 3.7 [⋆]	13.7 ± 3.7 [⋆]
α [g]	0.72	0.62
ϕ [degree] [h]	62	11
Flux [×10⁻¹⁶ erg s⁻¹ cm⁻²] [i]	17.8 ± 0.1	0.77 ± 0.03
Luminosity [×10⁴³ erg s⁻¹] [j]	20.55 ± 0.16	1.00 ± 0.03
$\bar{\sigma}_v$ [km s⁻¹] [k]	770 ± 2	352 ± 7
$\bar{\sigma}_g$ [km s⁻¹] [l]	560 ± 15	455 ± 55

Notes. [a]Line peak wavelength from the Gaussian modelling of Lyα- and CIV-CEN spectrum. [b]Redshift of the CEN corresponding to $\lambda_{\rm CEN}$. We used as Lyα and CIV λ rest-frame 1215.67 Å and 1549.48 Å, respectively. [c]Maximum projected physical size derived from the 3D-mask. [d]Spectral width within which the CEN was detected (from 3D-mask). [e]Distance from the quasar position to the SB peak of the CEN. [f]Distance from the quasar position to the flux weighted centroid of the CEN. [g]Asymmetry parameter, i.e. the ratio between the semi-minor and semi-major axis of the SB map. [h]Position angle east of north of the major axis of the SB map. [i]Total flux derived from the SB maps (Figs. 1 and 4). [j]Total CEN luminosity. [k]Averaged velocity dispersion measured from the $S/N \geq 3$ velocity dispersion maps (see Sect. 4.3) of the Lyα and CIV. [l]Velocity dispersions derived from the Gaussian fit of the total Lyα- and CIV-CEN spectrum. [⋆]Errors according to the spatial resolution of MUSE data.

consistency with morphological properties reported by AB19 in the QSO MUSEUM sample. Indeed, both the flux-weighted centroid shift and the asymmetry measured for the Lyα-CEN around J1538+08 are close to the median values reported in AB19, that is, 8.3 kpc and 0.71, respectively. The Lyα-CEN exhibits a maximum SB value of ∼10⁻¹⁶ erg s⁻¹ cm⁻² arcsec⁻² and a total luminosity of $L_{\rm Ly\alpha} = (2.06 \pm 0.02) \times 10^{44}$ erg s⁻¹.

The comparison between the Lyα spectra of the quasar and the CEN normalised to their peak emission is shown in Fig. 2. The quasar spectrum was extracted from an aperture with a radius of 3 arcsec, while the CEN spectrum was obtained from the PSF, and continuum, subtracted datacube by summing the spectral contribution of all the spaxels belonging to the CEN (i.e. from the 3D-mask). The x-axis reports the velocity relative to $z_{\rm QSO}$. The white area in the plot corresponds to the spectral width where the CEN was detected (i.e. the maximum spectral extent of the 3D mask; see also Table 1). The red area marks the peak of the Lyα profile of the CEN and includes the errors. The measure of the peak has been obtained through a Gaussian modelling plus a constant continuum term, performed within a range ±500 Å (or ±27 000 km s⁻¹) from the Lyα wavelength at $z_{\rm QSO}$. This peak appears to be reasonably (i.e. at ∼1σ) consistent with the $z_{\rm QSO}$ and its 1σ uncertainty (yellow area in Fig. 2).

Figure 3 reports the circularly averaged radial SB profile of the Lyα-CEN in J1538+08 (black points), which was corrected for minimal residual background emission[1]. The profile

---
[1] Similar to B16, the SB is estimated at scales much larger than the CEN and the profile is corrected for possible residual background due to unresolved and faint background or foreground (see Appendix A) emission that was not removed during the continuum subtraction. This
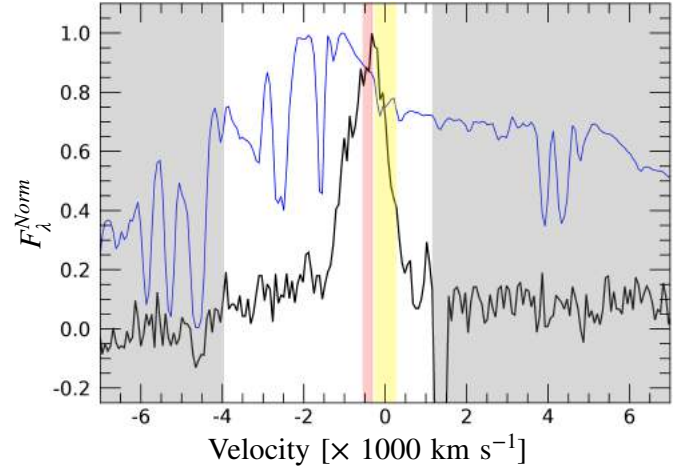
Fig. 2. Black and blue represents the Lyα emission lines in the CEN and quasar spectrum, respectively. These Lyα line spectra are reported in velocity space relative to the $z_{\rm QSO}$ and they both are normalised to their peak. The white region reports the spectral range of the 3D-mask. The red area marks the peak wavelength of the Lyα line derived through Gaussian modelling including the errors. The yellow area indicates the 1σ uncertainty of the systemic redshift of the quasar (Vietri et al. 2018). The absorption line at ∼1500 km s⁻¹ is a sky feature, which could not be appropriately removed by the algorithm CubePSFSub.

was extracted from concentric annular regions centred on the quasar position in the image obtained by collapsing the spectral region in the CEN 3D-mask. The grey area indicates the 2σ Poisson noise[2]. The radial profile was compared to the average radial profiles reported by B16 and AB19. All of the SB radial profiles in Fig. 3 were corrected for the cosmological $(1 + z)^4$ SB dimming factor and re-scaled at z=3 for comparison purposes.

We also report the rescaled profile of the CEN around the quasar J0124+00 (also belonging to the WISSH quasar sample, e.g. Duras et al. 2017), which was identified by B16 as the brightest and most peculiar one in their sample in terms of sharp-peaked morphology, large velocity dispersion, and SB radial profile. Both the Lyα-CEN around these WISSH quasars exhibit a central (i.e. <40–50 kpc) SB excess relative to the B16 and AB19 average profiles.

We further investigated the origin of this SB excess in J1538+08 by comparing the radial profiles extracted for two regions, that is, south and north of the quasar, which are delimited by the green dashed lines in Fig. 1. Accordingly, the southern region includes the SB peak of the Lyα-CEN and the CIV-CEN (see Fig. 4). The SB excess is clearly due to the contribution from the southern region (blue triangles in Fig. 3) at ≤20 kpc, while both regions equally contribute to the SB excess at larger radii.

4.2. CIV nebula

We scanned the datacube searching for diffuse emission in additional ionic transitions that typically probe the CGM. The only

---
subtraction, which was performed for both the Lyα and the CIV profiles (see Sect. 4.2), was measured to be negligible accounting for 5–15% of the flux of the most external annuli (used for the SB profile) placed at the boundary of each CEN.

[2] The Poisson noise was estimated as the average value of the standard deviations within background regions 1″×1″ of the pseudo-NB divided by the square root of each annulus area.
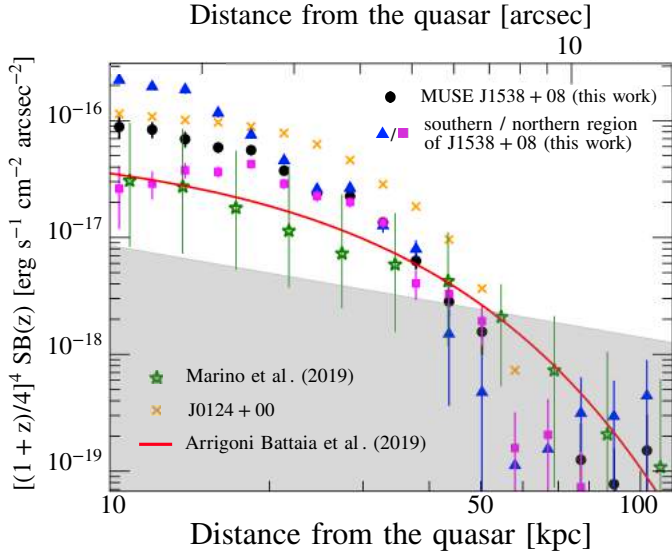
Fig. 3. Lyα SB radial profile (black circles) of the pseudo-NB image. The points represent bins of SB measured in concentric annuli centred on the quasar position and their errors indicate the 16th and 84th percentile, which corresponds to ~68% of the SB distribution centred on the median value (i.e. ±1σ for a Gaussian distribution). The bin width is chosen to be uniformly spaced in a logarithmic scale. The blue triangles and magenta squares show the radial profiles measured in the southern and northern region of the CEN, respectively (see Fig. 1). The red curve is the modelled average radial profile of the AB19 quasar sample. We also include the average radial profile of the Lyα-CEN of the sample of B16, which was recalculated by Marino et al. (2019) (the error bars represent the 25th and 75th percentiles). The orange crosses represent the radial profile of the Lyα-CEN around the WISSH quasar J0124+00 in the B16 sample. All the SB profiles were corrected for the cosmological dimming effect and re-scaled at $z = 3$ (i.e. $[(1 + z)/4]^4 \times SB(z)$). The grey shaded area indicates the 2σ Poisson noise relative to the rescaled profiles of the Lyα-CEN around J1538+08 (see Sect. 4.1 for details). We verified that the decline of the SB radial profile from the northern region (magenta squares) at short radius towards the centre is not due to the white region immediately north of the quasar (see Fig. 1).

extended emission detected at a good significance level is traced by the CIV line. Given its typically lower emissivity compared to the Lyα, we started our search by setting $S/N_{th} = 2.5$ and $N_{th}^{vox} = 10\,000$ and then progressively lowered N_{th}^{vox} by steps of 1000 voxels until the extended emission was detected. We found that the $N_{th}^{vox} = 4000$ was required to detect this CEN, which indeed consists of 4726 voxels.

The SB map of the CIV-CEN is shown in Fig. 4. The CIV-CEN is much smaller than the Lyα-CEN, with a maximum angular extension of ~10 arcsec, which corresponds to a projected physical size of ~75 kpc. It is almost completely contained in the southern region and exhibits an asymmetric morphology with $\alpha = 0.62$. The peak of the SB_{CIV} is located roughly at the same position of the $SB_{Ly\alpha}$ peak at a distance of ~11.0 ± 3.5 kpc from the quasar position. The value of the SB peak (~10^{-17} erg s^{-1} cm^{-2} arcsec^{-2}) and the luminosity of the CIV-CEN ($L_{CIV} = (9.33 \pm 0.33) \times 10^{42}$ erg s^{-1}) are one order of magnitude lower than those measured for the Lyα-CEN.

Figure 5 shows the comparison between the CIV emission line in the CEN and the quasar spectrum. The CIV-CEN was detected in a relatively narrow spectral range (~2000 km s^{-1}) compared to the spectral region of the Lyα-CEN (~5000 km s^{-1}). Through Gaussian modelling of the line (similar to the one performed for the Lyα), we found that the CIV line peaks at
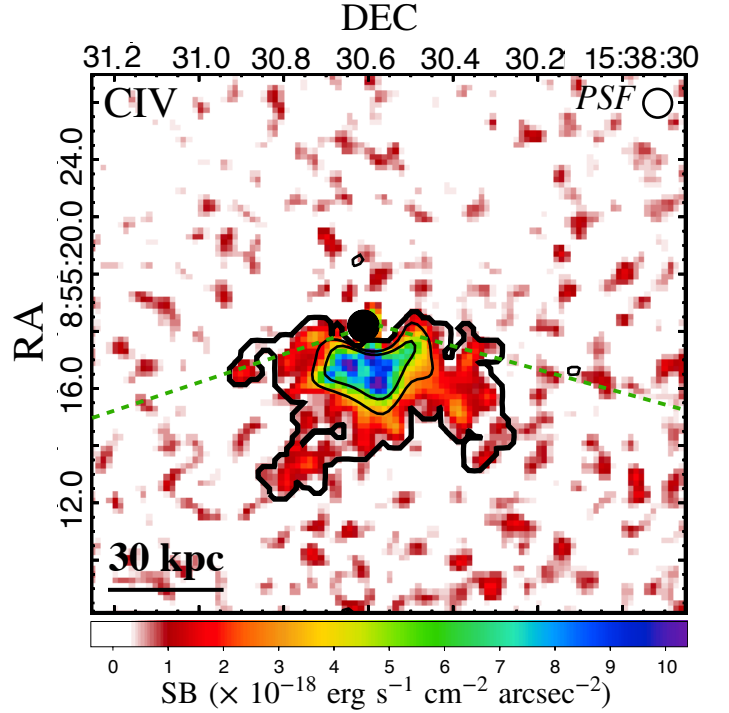
Fig. 4. Optimally extracted SB map of the CIV-CEN. The black dot, the contours, and the dashed green lines have the same meaning as in Fig. 1. Thin contours report levels of $S/N = 3$ and 5.
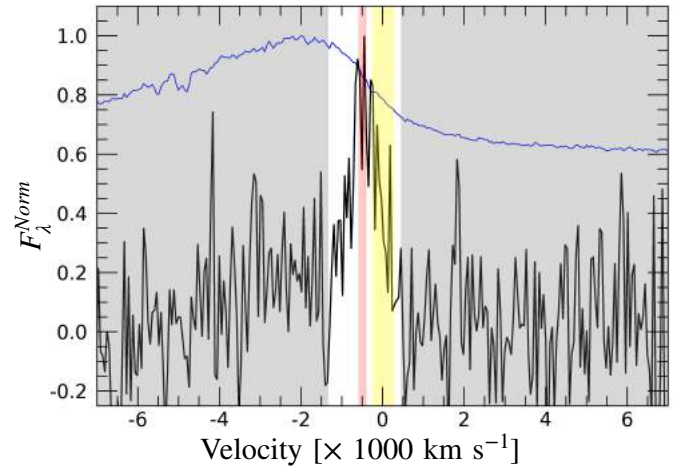

Fig. 5. Spectrum of the CIV emission as a function of the velocity with respect to the quasar redshift of the CIV-CEN (black) and quasar (blue) normalised to their peak emission. Labelling and symbols are the same as in Fig. 2.

$\lambda_{CIV}^{CEN} = 7064.7 \pm 1.8$ Å. This corresponds to a redshift of $z_{CEN}^{CIV} = 3.559 \pm 0.001$, which is in good agreement with the Lyα-CEN one. We computed the SB radial profile of the CIV emission (Fig. 6) in the southern region. The emission of the CEN is clearly above the Poisson noise up to ~20 kpc from the quasar position.

4.3. Kinematic properties of the CEN

Figures 7 and 8 show the flux-weighted velocity maps in regions with $S/N \geq 3$ for the Lyα- and CIV-CEN, respectively. Each panel reports the velocities relative to the CEN (z_{CEN}; left panel) and z_{QSO} (right panel) rest-frame, respectively. There is
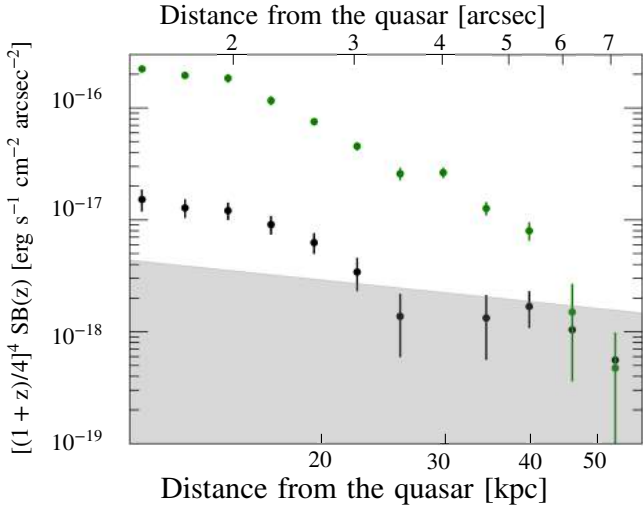
Fig. 6. SB radial profile of the CIV-CEN (black) extracted in the southern region (see Fig. 4). The SB profile for the Lyα-CEN, extracted in the same region, is also reported in green. These profiles are re-scaled at $z = 3$ and corrected for the cosmological dimming effect. For other details refer to the caption of Fig. 3.

no significant structure indicative of bulk motion or clear separation between red and blueshifted gas components. Interestingly, almost the entire Lyα-CEN exhibits velocities spanning $\sim 1000\,\mathrm{km\,s^{-1}}$.

We also investigated the radial velocity profile of the Lyα-CEN to assess a possible trend with the distance from the quasar. Specifically, we extracted spectra from the PSF- and continuum-subtracted datacube in each annular region used for the SB radial profiles (see Fig. 3). For each spectrum, we modelled the Lyα emission line with a Gaussian profile. Figure 9 shows the radial distribution of the best-fit velocities relative to the z_{CEN} (blue points). The velocity profile exhibits a constant value around $\sim 100-200\,\mathrm{km\,s^{-1}}$ up to 15–20 kpc. There is an apparent decline of the velocity down to $-200\,\mathrm{km\,s^{-1}}$ at larger radii (20–30 kpc).

The flux-weighted velocity dispersion maps for Lyα- (left panel) and CIV-CEN (right panel) are shown in Fig. 10. For the Lyα-CEN, we do not notice any specific gradient as the map shows a nearly constant σ_{v} in the range of 600–900 km s^{-1} with few regions reaching values larger than 1000 km s^{-1}. In case of the CIV-CEN, the map shows a factor of 2 lower velocity dispersions than the Lyα-CEN. Table 1 lists the average velocity dispersions ($\bar{\sigma}_{\mathrm{v}}$) obtained from these maps. The dispersion estimated through Gaussian model fitting ($\bar{\sigma}_{\mathrm{g}}$) of the total spectrum of the Lyα- and CIV-CEN is also reported.

In order to better explore the possible presence of a radial gradient of the Lyα emission velocity dispersion, we computed the radial dispersion profile by using the same methodology adopted for the velocity profile (see red points in Fig. 9). The profile exhibits $\sigma_{\mathrm{v}} \sim 500\,\mathrm{km\,s^{-1}}$ up to $\sim 15-20$ kpc and an increase of up to $\sigma_{\mathrm{v}} \sim 900\,\mathrm{km\,s^{-1}}$ at ~ 25 kpc from the quasar. The profiles could only be accurately computed up to 40 kpc since the line profile modelling at larger distances is completely unconstrained.

4.4. CIV/Lyα and HeII/Lyα line ratios

We derived a CIV/Lyα line flux ratio of 0.06 ± 0.01, which is in agreement with the approximate values previously estimated for some tentative ($\sim 2.2\sigma - 2.8\sigma$) detections of CIV-CEN in B16.

Similar to our result, the B16 values were obtained by estimating the total flux of the voxels associated with the Lyα 3D-Mask shifted at the wavelength of the CIV corresponding to z_{CEN}, which was divided by the total flux of the Lyα-CEN (reported in Table 1). This procedure avoids the bias due to aperture effects (i.e. different extensions for different line emissions), and it provides a conservative estimate if the Lyα-CEN is the brightest and more extended one, which is to be expected.

The CIV/Lyα ratio map reported in Fig. 11 is the ratio between the CIV and Lyα SB maps over the $S/N \geq 3$ regions. The spatial distribution of the ratios suggests that the metal distribution is not completely homogeneous. The median value of the CIV/Lyα ratio directly measured from the CIV/Lyα map is $0.08^{+0.11}_{-0.04}$, where the uncertainties are derived by the 16th and 84th percentiles (corresponding to $\pm 1\sigma$ for a Gaussian distribution). A consistent value was obtained by computing the S/N-weighted average of the map values of both Lyα- and CIV-CEN.

No HeII emission line is visible in the quasar spectrum and no HeII-CEN is detected around J1538+08 at z_{CEN}. This is not surprising: While extended HeII emission is commonly observed around high-redshift radio galaxies (e.g. Wilman et al. 2000; Villar-Martín et al. 2007a), it is only found in 6% of the RQQs in the B16 sample. We inferred a 2σ upper limit to the HeII/Lyα ratio of <0.02 by applying the same Lyα 3D-mask shift procedure used to obtain the total CIV/Lyα flux ratio.

4.5. Asymmetry in Lyα line profile

The integrated profile of the Lyα emission line extracted from the entire CEN and reported in Fig. 2 exhibits a blue tail, which can be modelled by an additional component with negative velocity. With the aim of exploring the spatial distribution of this blue tail component, we mapped the asymmetry of the Lyα emission line profile by using the skewness estimator (sk). As for the velocity and dispersion maps, we derived the skewness map as the third moment of the flux distribution according to the following formula:

$$\mathrm{skewness} = \frac{\sum_{i,j,k}^{\mathrm{3D\text{-}Mask}} \mathrm{Residuals}_{i,j,k}^3 \times F_{i,j,k}}{M_2^{3/2} \times \sum_{i,j,k}^{\mathrm{3D\text{-}Mask}} F_{i,j,k}} \qquad (1)$$

where $\sum_{i,j,k}^{\mathrm{3D\text{-}Mask}}$ is the sum on each voxel defined in the 3D-Mask, $F_{i,j,k}$ is the PSF and continuum-subtracted flux from the datacube, and M_2 is the second moment of the flux distribution, defined as:

$$M_2 = \frac{\sum_{i,j,k}^{\mathrm{3D\text{-}Mask}} \mathrm{Residuals}_{i,j,k}^2 \times F_{i,j,k}}{[\sum_{i,j,k}^{\mathrm{3D\text{-}Mask}} F_{i,j,k}]^2 - [\sum_{i,j,k}^{\mathrm{3D\text{-}Mask}} F_{i,j,k}^2]} . \qquad (2)$$

We find that the southern part of the CEN, which has skewness values of $sk < -0.5$ (blue regions in Fig. 12), overlaps with the region of high SB. We verified that other regions do not exhibit skewness at significant levels (i.e. mostly symmetric and low S/N line profiles). The Lyα spectrum extracted from spaxels with $sk < -0.5$ and $S/N \geq 3$ resulted to be clearly asymmetric (Fig. 13). We fitted it with two Gaussian components and an additional constant term to account for residual background. The two Gaussian components exhibit significantly different width, with the broad ($\sigma_{\mathrm{v}} \simeq 1170 \pm 260\,\mathrm{km\,s^{-1}}$) component blueshifted by $v_{\mathrm{shift}} = 1520 \pm 360\,\mathrm{km\,s^{-1}}$ and the narrow one ($\sigma_{\mathrm{v}} \simeq 470 \pm 70\,\mathrm{km\,s^{-1}}$, see Table 2) tracing the systemic z_{QSO}. The velocity dispersion found for the narrow component is comparable to the ones reported in Lyα-CEN around high-z RQQs
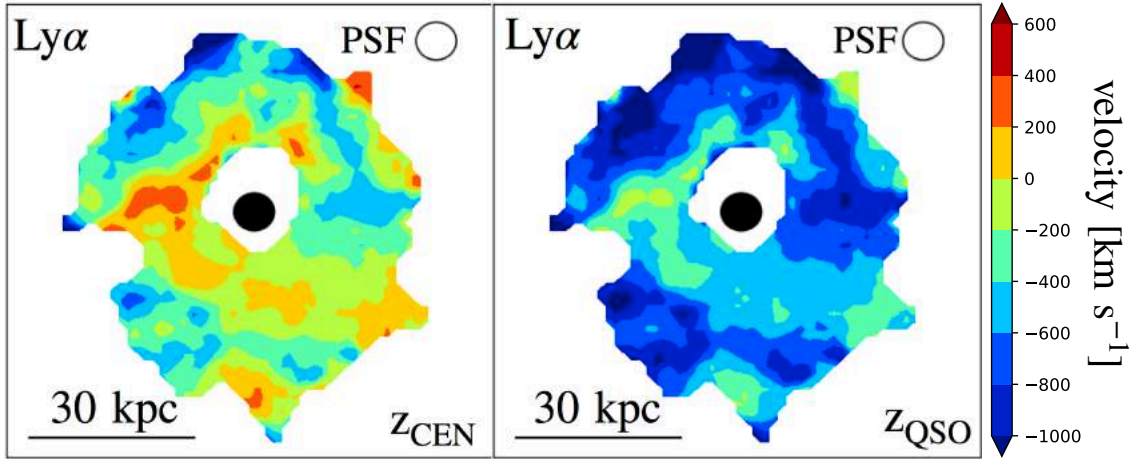
Fig. 7. Flux-weighted velocity maps of the Lyα-CEN for $S/N \geq 3$ regions relative to z_{CEN} (*left*) and to z_{QSO} (*right*).
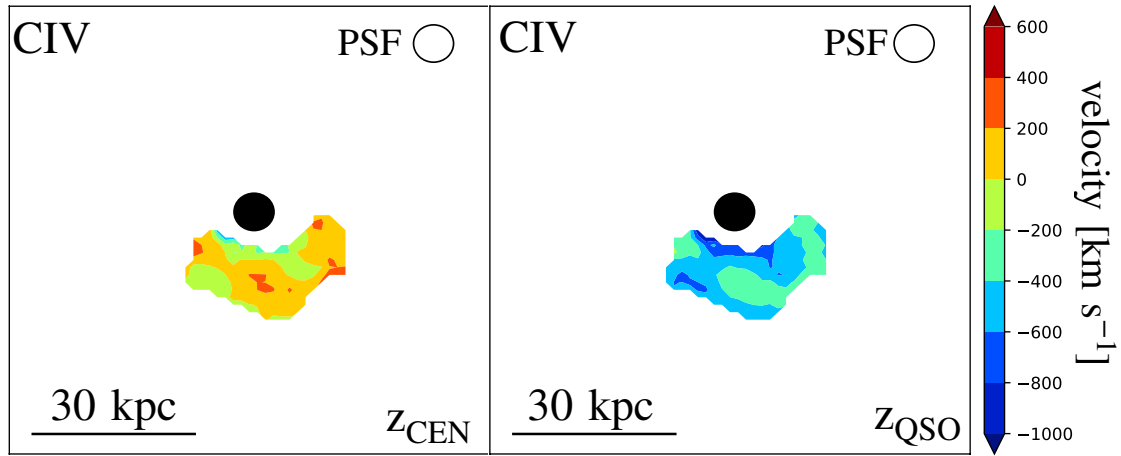
Fig. 8. Flux-weighted velocity maps for $S/N \geq 3$ regions of the CIV-CEN. As in Fig. 7, the *right and left panels* show the velocity relative to z_{CEN} and to z_{QSO}, respectively.
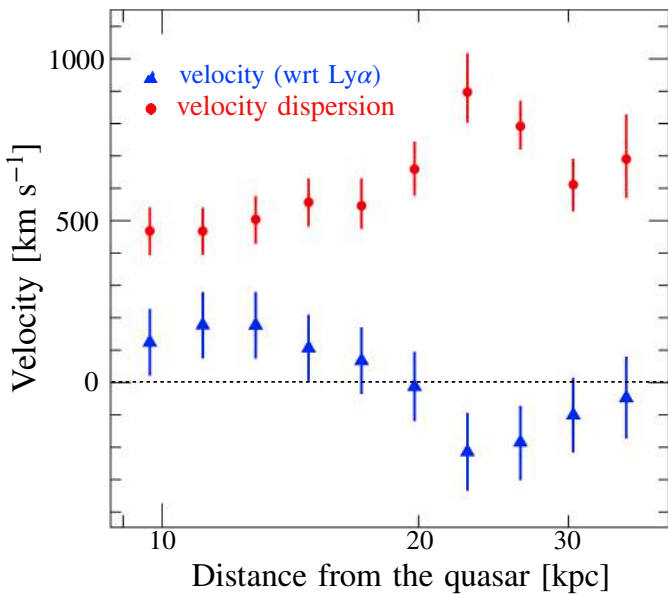
Fig. 9. Radial profile of velocity (blue triangles) and dispersion (red circles) derived from the modelling of a single Gaussian of the Lyα profiles extracted in concentric annular region centred on the quasar position.

(e.g. B16; AB19). The centroid of the narrow component corresponds to a redshift of $z \sim 3.562 \pm 0.001$, which is consistent with z_{QSO}.

5. Discussion

5.1. Comparison with the properties of other Lyα-CEN samples

We have reported the discovery of a Lyα-CEN around the hyperluminous RQQ J1538+08, which exhibits a projected size of $\sim$150 kpc and a luminosity of $L_{Ly\alpha} \sim 2 \times 10^{44}$ erg s^{-1}. Previous MUSE studies at similar redshifts (i.e. $z \sim 3$–4) and exposures (0.75–1 h) reported Lyα-CEN around similarly luminous RQQs (B16) and quasars with slightly lower L_{bol} (AB19). The Lyα-CEN around J1538+08 exhibits a maximum projected size, which is similar to the average value ($\sim$150 kpc) found for the B16 sample, while its luminosity is one of the highest measured thus far (see Fig. 14) and it is comparable to the luminosity of the known ELANe (e.g, Cantalupo et al. 2014; Hennawi et al. 2015; Cai et al. 2017b; Arrigoni Battaia et al. 2018).

The SB$_{Ly\alpha}$ radial profile of our CEN, shown in Fig. 3, exhibits a projected distance from the quasar at a SB of $\sim$10^{-18} erg s^{-1} cm^{-2} arcsec^{-2} (i.e. $\sim$50 kpc), which is similar to the one inferred from the average profiles from B16 and AB19.
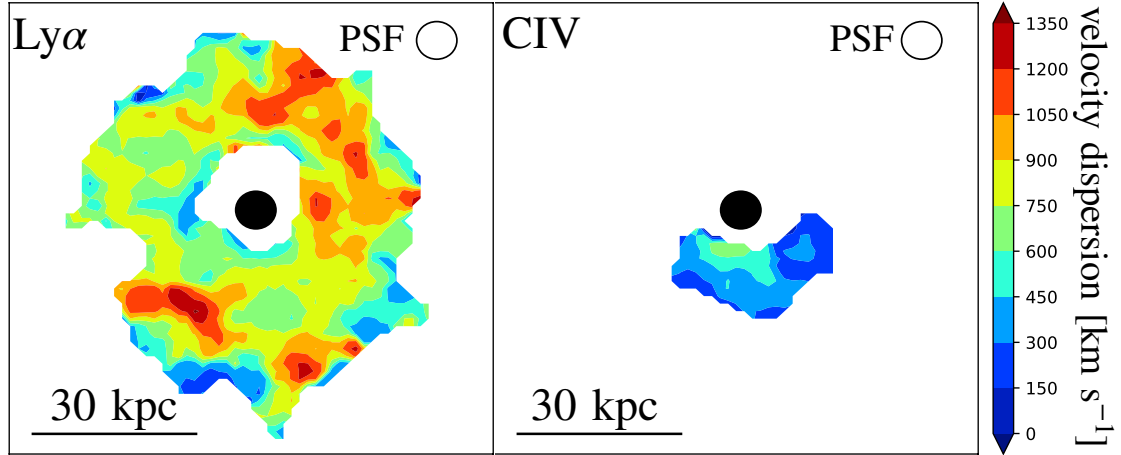
Fig. 10. Flux-weighted velocity dispersion maps for Lyα- (*left*) and CIV- (*right*) CEN. The MUSE spectral resolution in these dispersion maps is $\approx 70\,\mathrm{km\,s^{-1}}$.
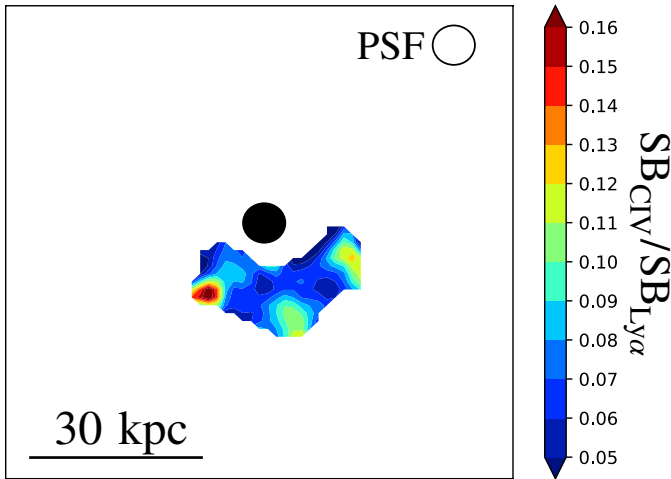
Fig. 11. Map of the CIV/Lyα SB ratio. Only regions with $S/N > 3$, for both the Lyα- and CIV-CEN, are displayed.
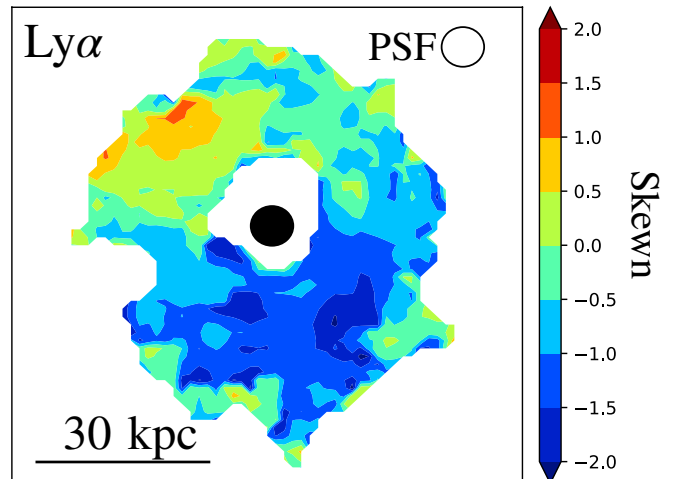
Fig. 12. Skewness map of the line profile of the Lyα-CEN.

This behaviour seems to be independent of the luminosity of the quasar (AB19). However, it is important to notice that the SB at this distance coincides with the level of the 2σ Poisson noise of the image and, therefore, deeper observations are needed in order to verify this claim.

Interestingly, some WISSH quasars are included in the B16 (J0124+00, J1621−00), AB19 (J0125−10, J0947+14), and Cai et al. (2019) (J2123−00) samples. The size and luminosity of the Lyα-CEN detected around them appear to be heterogeneous (see Fig. 14), suggesting that the properties of these CEN have no simple dependence on the similar, large quasar radiative output (i.e. $L_{\mathrm{bol}} > 10^{47}\,\mathrm{erg\,s^{-1}}$).

We also checked for possible dependencies on the RQQs bolometric and 2500 Å luminosities (derived from spectral energy distribution modelling; Duras et al. 2017, and in prep.) to verify if the nuclear radiative output could affect the properties of the Lyα-CEN around the WISSH quasars considered here. However, no significant trend with luminosity was observed, confirming the result reported by AB19 for a larger sample of quasars.

### 5.2. Kinematics of the Lyα- and CIV-CEN of J1538+08

From the velocity maps of the Lyα- and CIV-CEN (Figs. 7 and 8), no coherent kinematic structures that possibly hint at bulk motions

and rotations were detected. However, the velocity map of the Lyα-CEN exhibits a large fraction ($79^{+9}_{-10}\%$)[3] of pixels with $S/N \geq 3$ with negative velocities relative to z_{CEN}. This can be justified by the presence of the additional blueshifted component in the Lyα line profile (see Sect. 4.5 and Fig. 2). For the CIV-CEN, where we did not detect any significant additional component, the velocity map shows a roughly equal number of pixels with negative and positive velocities. Interestingly, by adopting z_{QSO} as a reference redshift for the velocity maps of the Lyα- and CIV-CEN, we find that ~100% of the $S/N \geq 3$ pixels have negative velocities. Furthermore, our Lyα-CEN shows a peak with a negative velocity of $-438 \pm 267\,\mathrm{km\,s^{-1}}$. This can be an indication that our z_{QSO} estimated from the Hβ may suffer from systematic uncertainties. Indeed, for a sample of 849 quasars, Shen et al. (2016) find that the determination of the quasar redshift from Hβ is subject to uncertainties as large as ~400 km s^{-1}. This can compensate the reported negative velocity offsets of the Lyα peak and the velocity distribution of the $S/N \geq 3$ pixels at levels of ~1−2σ.

Regarding the velocity dispersion, we measured a spatially averaged value $\bar{\sigma}_{\mathrm{v}} = 733 \pm 85\,\mathrm{km\,s^{-1}}$ from the dispersion map (see Table 1). This is a factor of two larger than those measured

---

[3] Errors were derived from the uncertainties to the redshift of both the quasar and nebula.
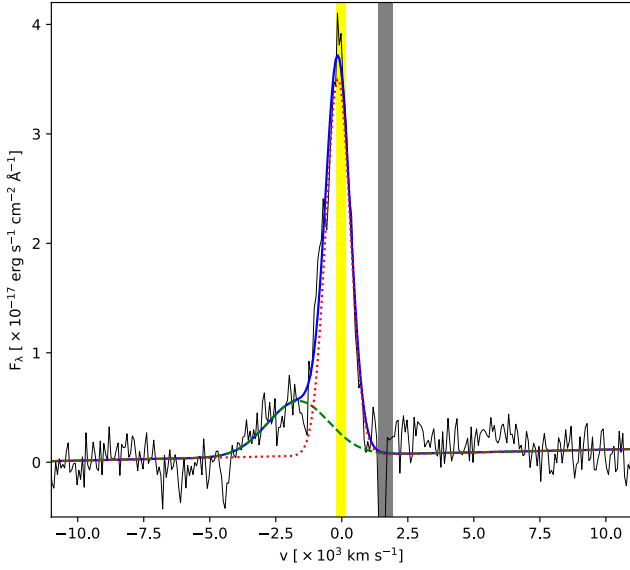
Fig. 13. Lyα spectrum extracted from the CEN region with $sk < -0.5$ and $S/N > 3$ and modelled (blue solid line) by two Gaussian components (red dotted and green dashed lines). Interestingly, the broad ($\sim$1170 km s^{-1}) wing is blueshifted by $\sim$1520 km s^{-1} from the narrow component. The grey area is not considered in the modelling as it includes a region contaminated by a sky feature. The yellow region reports the $\pm 1\sigma$ uncertainty on the z_{QSO}.

Table 2. Properties derived from the two-component Gaussian fit of the Lyα-CEN spectrum extracted from regions with $S/N \geq 3$ and $sk < -0.5$.

Components	Narrow	Broad
λ_{cen} [Å]	5546.3 ± 1.3	5518.3 ± 6.5
σ_v [km s^{-1}]	470 ± 70	1170 ± 260
Flux $^{(a)}$ [$\times 10^{-16}$ erg s^{-1} cm^{-2}]	7.4 ± 0.7	2.7 ± 0.9
v_{shift} $^{(b)}$		(1520 ± 360) km s^{-1}
v_{max} $^{(c)}$		(3860 ± 870) km s^{-1}
χ^2/d.o.f.		$402/366$

Notes. $^{(a)}$Integrated fluxes of the narrow and broad Gaussian components. $^{(b)}$Velocity offset between the positions of the broad and narrow components. $^{(c)}$Maximum velocity of the blueshifted, broad component defined as $v_{max} = v_{shift} + 2\sigma_v$, where σ_v is the dispersion derived for the broad component.

around the quasars of B16 and AB19 samples, which span the range of $\sigma_v \approx [200, 400]$ km s^{-1}. This value is more similar to the reported values for Lyα-CEN around high-z radio galaxies in the regions affected by radio jets ($\sigma_v \gtrsim 600$ km s^{-1}; van Ojik et al. 1997; Villar-Martín et al. 2003; Humphrey et al. 2006; Silva et al. 2018).

Interestingly, the dispersion map of the Lyα-CEN around J1538+08 reports several discrete and compact regions with very high $\sigma_v \approx 1000$ km s^{-1} at an average distance from the quasar of 20–30 kpc (see Fig. 10). These high σ_v regions could be due to the turbulence generated by continuum or line-emitting active sources at z_{CEN}, which possibly inject energy into the CGM. However, no continuum sources in the MUSE FOV are associated with high σ_v values within the Lyα-CEN. Similar to AB19, we used `CubExtractor` to search for Lyα emitters by setting $S/N_{th} > 5$ and $N^{vox}_{min} = 50$. We did not detect any source within the CEN. We only found a source with a flux of 3.5×10^{-16} erg s^{-1} cm^{-2}, at the redshift of the CEN ($z \approx 3.560$),
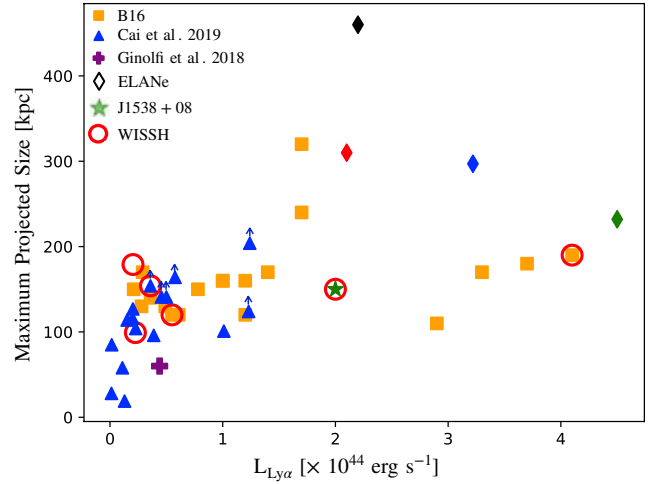
Fig. 14. Maximum projected size versus luminosity of the Lyα-CEN around J1538+08 (green star) and around quasars from the B16 (orange squares), Cai et al. (2019) (blue triangles) and Ginolfi et al. (2018) (purple cross) samples. The values for the ELANe (diamond symbols) detected by Cantalupo et al. (2014) (black), Hennawi et al. (2015) (red), Cai et al. (2017a) (green), and Arrigoni Battaia et al. (2018) (blue) are also included. WISSH quasars are marked with an additional red circle. We also report the two Lyα-CEN around the WISSH quasars from the AB19 sample, i.e. those with the lower luminosities. For these two Lyα-CEN, the maximum distance from the quasar spanned by the Lyα emission within the 2σ isophote multiplied by a factor of two is shown since AB19 do not report the values of the maximum projected size.

outside its boundaries and at a projected distance of $\sim$250 kpc from the quasar (RA = 15:38:28.7, Dec = +8:55:00.80), which very likely cannot affect the nebular emission.

5.3. Metals in CGM

The CIV-CEN revealed around J1538+08 is one of the few extended (75 kpc) CIV-emitting regions detected at high significance (5σ)[4] and spatially mapped around a RQQ. This provides a clear indication of a metal enriched medium (i.e. non-pristine) around this quasar. The luminosity of this CEN ($L_{CIV} \simeq 10^{43}$ erg s^{-1}) is comparable to those measured for CIV-CEN detected around radio galaxies at similar redshift (Villar-Martín et al. 2007a). However, its morphology shows a marked asymmetry relative to the central quasar position. This is at odds with symmetrically distributed CEN reported around radio galaxies (e.g. Villar-Martín et al. 2007b; Silva et al. 2018). Interestingly, the ratio between the SB radial profiles of the CIV and Lyα reported in Fig. 6 (i.e. in the southern wedge containing the SB Lyα peak and the CIV-CEN) is a factor of $\sim$0.1 and is constant up to $\sim$25 kpc (i.e. the distance where the Poisson noise starts to dominate the CIV-CEN radial profile). This evidence and the spatial co-location of the SB peaks of the two CEN suggest that they could trace the same gas and, hence, be triggered by the same mechanism. Deeper observations would hopefully reveal fainter CIV emission with the same size and morphology of the Lyα-CEN in J1538+08.

5.4. Powering mechanisms for the Lyα CEN

The possible powering mechanisms of the Lyα-CEN include quasar photoionisation (i.e. fluorescence), collisional excitation

---

[4] This value represents the integrated S/N computed for the extended CIV emission line.

(i.e. cooling), and shocks. In the case of fluorescence, assuming that the quasar is surrounded by cold and spherical clouds, we can estimate the CEN SB in the following two extreme regimes: optically thin (with a column density of $N_{\rm H} \ll 10^{17.2}\,{\rm cm}^{-2}$) and optically thick ($N_{\rm H} \gg 10^{17.2}\,{\rm cm}^{-2}$; Hennawi & Prochaska 2013). We obtain $SB_{\rm Ly\alpha}^{\rm thick} \simeq 2.8 \times 10^{-15}\,{\rm erg\,s\,cm}^{-2}\,{\rm arcsec}^{-2}$ and $SB_{\rm Ly\alpha}^{\rm thin} \simeq 2.2 \times 10^{-18}\,{\rm erg\,s\,cm}^{-2}\,{\rm arcsec}^{-2}$, for optically thick[5] and optically thin[6] gas, respectively. In our case, we find that $SB_{\rm Ly\alpha}$ for regions with $S/N \geq 3$ is $\simeq 2.3 \times 10^{-17}\,{\rm erg\,s\,cm}^{-2}\,{\rm arcsec}^{-2}$. This value is more compatible with $SB_{\rm Ly\alpha}^{\rm thin}$ than with $SB_{\rm Ly\alpha}^{\rm thick}$, supporting the presence of an optically thin medium as already reported in previous works (e.g. AB19; Cai et al. 2019).

The CIV/Lyα and HeII/Lyα ratios could be used to understand if shocks or collisional excitation are viable powering mechanisms for the observed Lyα-CEN (but see Cantalupo et al. 2019). The detection of the CIV-CEN allows us to rule out cooling due to gravitational accretion as the powering mechanism of this CEN. However, it is notoriously difficult to disentangle photoionisation models from shock models in a HeII/Lyα versus CIV/Lyα diagram (Arrigoni Battaia et al. 2015a). Nevertheless, photoionisation models usually do not predict lower levels of HeII/Lyα with respect to CIV/Lyα (e.g. Humphrey 2019; Cantalupo et al. 2019). On the contrary, they predict ratios of the same order for the two transitions. This is because these two emission lines have similar ionisation energies, 64.5 eV for CIV and 54.4 eV (4 Ryd) for HeII. On the other hand, shock models (Allen et al. 2008) do show cases in which the HeII/Lyα ratio is lower than the CIV/Lyα ratio. Indeed, according to shock and precursors models presented by Allen et al. (2008) and Arrigoni Battaia et al. (2015b) regarding the origin of extended nebular emission, the values of CIV/Lyα and HeII/Lyα inferred from our analysis are consistent with a shock propagating at 200–300 km s^{-1} in a $n_{\rm H} \sim 10$–$100\,{\rm cm}^{-3}$ gas or with a faster >1000 km s^{-1} shock in a denser gas ($n_{\rm H} > 100\,{\rm cm}^{-3}$). If we assume that the $v_{\rm shift} = 1520$ km s^{-1} is the velocity of the shock, then the emitting gas is required to be at high densities ($n_{\rm H} > 100\,{\rm cm}^{-3}$).

The aforementioned photoionisation and shock models do not include a contribution from resonant scattering of Lyα photons from the quasar. In a case in which such a contribution is important, the CIV/Lyα and HeII/Lyα ratios predicted by those models need to be corrected and shifted to lower values. However, it has been shown that the efficient diffusion in velocity space allows the Lyα resonantly scattered photons, which were produced by the quasar itself, to escape the system at very small scales of <10 kpc (Dijkstra et al. 2006). Therefore, this should result in a negligible contribution of scattered Lyα emission on scales >10 kpc (e.g, Cantalupo et al. 2014). A firm characterisation of the Lyα resonant scattering contribution requires a full radiative transfer calculation on a three dimensional gas distribution that represents this system. This approach is beyond the scope of this work.

5.5. Evidence of outflowing gas in the CGM

The blueshifted broad component in the Lyα spectrum of the CEN provides tantalising evidence for the presence of

outflowing gas reaching a projected distance of 20–30 kpc from the quasar, that is, into the CGM surrounding J1538+08. The latter also exhibits a host-galaxy scale [OIII] outflow with a mass outflow rate of $\sim 530\,M_\odot\,{\rm yr}^{-1}$, a maximum velocity of ~ 2900 km s^{-1}, and kinetic power of $\dot{E}_{\rm kin} = 1.4 \times 10^{45}$ erg s^{-1} (see Vietri et al. 2018). In an energy conserving scenario in which the large-scale outflow reported in this paper is in the later stage of the AGN-driven [OIII] one (e.g. Bischetti et al. 2017; Vietri et al. 2018), by assuming an expansion at $v_{\rm out} = v_{\rm shift} \sim 1500$ km s^{-1}, we estimated a mass outflow rate of $\dot{M}_{\rm out} \simeq 300\,M_\odot\,{\rm yr}^{-1}$, which is comparable to the [OIII] one. It is important to notice that, assuming $v_{\rm out} = 300$ km s^{-1} as suggested by the CIV/Lyα and HeII/Lyα values in shock+precursor models, (see Sect. 5.3) we would obtain a $\dot{M}_{\rm out}$ that is larger by a factor of 25 but that is still comparable with the typical $\dot{M}_{\rm out}$ reported for [OIII] outflows in the WISSH sample (Bischetti et al. 2017). By assuming a constant velocity of 1500 km s^{-1} (see Table 2), we estimated that an outflow at host galaxy scales (i.e. ~ 5–10 kpc Bischetti et al. 2017) would take ~ 7–13 Myr to reach the distance of our CGM outflow (i.e. ~ 30 kpc). In adopting a velocity of ~ 300 km s^{-1}, we would obtain an upper limit to the outflow time a factor of 5 larger than the previous estimate.

The sudden increase of the velocity dispersion of the Lyα-CEN to $\sigma_{\rm v} \sim 900$ km s^{-1} at a distance of ~ 20 kpc (see Fig. 9) could be partially due to the presence of the outflow component and hence to an incorrect parameterisation of the line profile with a single Gaussian component. Unfortunately the S/N of our observations did not allow us to recompute the radial profile of the v and $\sigma_{\rm v}$ of the Lyα line using a two-component Gaussian modelling because the S/N of the broad Lyα line in each bin is too low. Deeper MUSE observations are therefore needed to verify the presence of a broad and blueshifted component over the entire Lyα-CEN and assess if the CIV-CEN also shares the same kinematics.

Given the resonant nature of the Lyα transition, complex radiative transfer models that account for the velocity field, the density structure of the CEN, and the geometry of the radiation field are needed in order to properly interpret the properties derived by the Lyα line profile fitting (e.g. Cantalupo et al. 2005; Gronke & Dijkstra 2016). It is worth noting that the presence of an expanding shell surrounding the quasar, assuming spherical symmetry and isotropic geometry of the photoionising radiation field, may produce an asymmetric double peak profile in which the blue-ward component is strongly suppressed (Verhamme et al. 2006; Laursen et al. 2009; Steidel et al. 2010; Chung et al. 2019). This would provide support to the hypothesis of an outflowing CEN whose two components of the Lyα profile are associated with the same expanding gas. It is important to notice that in this simple model (i.e. symmetric, homogeneous, and isotropic gas distribution), the main peak component is always on the red side compared to the systemic redshift of the CEN. However, assuming that $z_{\rm QSO} \equiv z_{\rm CEN}$, our Ly$\alpha$-CEN does not show such a red line component (see Fig. 13). To test the nature of this putative outflow in the context of an asymmetric, inhomogeneous gas distribution, MUSE observations with a higher S/N are needed along with a more accurate determination of $z_{\rm QSO}$ (e.g. from the CO line) and radiative transfer models.

6. Summary and conclusions

In this paper we have presented a VLT/MUSE investigation on the CGM around J1538+08, a $z \approx 3.6$, broad-line, RQQ belonging to the WISSH quasars sample (Bischetti et al. 2017). The main results can be summarised as follows.

---

[5] The luminosity at the Lyman edge, which is required by the formula (15) by Hennawi & Prochaska (2013), has been estimated by the L_{1450} (see Duras et al., in prep.) as detailed in Lusso et al. (2015) and Farina et al. (2019). Moreover, we adopted as a CEN radius, 40 kpc (see Fig. 3) and a covering factor $f_{\rm c} = 0.5$.

[6] We used the formula (10) in Hennawi & Prochaska (2013) and adopted the following fiducial values: $N_{\rm H} = 10^{20}\,{\rm cm}^{-2}$, density $n_{\rm H} = 0.1\,{\rm cm}^{-3}$, and $f_{\rm c} = 0.5$.

- We discovered a CGM emission nebula (CEN) detected in Lyα of ∼150 kpc surrounding J1538+08, which is among the most luminous Lyα-CEN ($\sim 2 \times 10^{44}$ erg s^{-1}) reported so far (Borisova et al. 2016; Arrigoni Battaia et al. 2019; Farina et al. 2019). Our nebula appears roughly symmetric on large scales (several tens of kiloparsecs) and exhibits a bright SB peak located at ∼10−15 kpc southwards of the quasar.

- We obtained one of the first 2D-mappings of a significantly detected ($\sim 5\sigma$), extended (∼75 kpc) CIV-CEN around a RQQ. Given its spatial coincidence with the Lyα SB peak and a similar SB profile, it is very likely associated with the Lyα-CEN.

- We find no significant velocity pattern in the kinematics of the Lyα-CEN. Remarkably, the average velocity dispersion $\bar{\sigma}_v \simeq 700$ km s^{-1} is higher than the typical values measured in RQQs and it is notably more similar to the dispersion observed for Lyα-CEN around high-redshift radio galaxies (van Ojik et al. 1997; Villar-Martín et al. 2003; Humphrey et al. 2006; Silva et al. 2018) and outflow-dominated systems (Ginolfi et al. 2018).

- We obtained one of the first 2D characterisation via IFU spectroscopy of an ionised outflow at CGM scales ($\gg 10$ kpc) around a RQQ by performing the spectral analysis of an extended region with a negative skewness value.

  Specifically, the analysis of the skewness map of the Lyα-CEN reveals a region within 30 kpc that is to the south of the quasar in which the skewness is negative (see Fig. 12); additionally, the Lyα emission profile is significantly asymmetric with a blue tail. This region roughly overlaps with the SB peak of the Lyα-CEN and includes the CIV-CEN.

  The Lyα spectrum that was extracted from the region showing negative skewness is well modelled with two Gaussian components (Fig. 13). This fit resulted into a systemic narrow ($\sigma_v \sim 500$ km s^{-1}) component and a broader ($\sigma_v \approx 1200$ km s^{-1}) one. The latter is blueshifted by $v_{\text{shift}} \simeq 1500$ km s^{-1} and is indicative of outflowing gas on CGM-scales.

All of the reported results clearly indicate the presence of a metal-enriched (i.e. non pristine) gas with kinematic features that are consistent with an outflowing gas component at scales of tens of kiloparsecs. Both deeper spatially resolved spectroscopic observations of the CGM around this hyper-luminous quasar and dedicated radiative transfer modellings are necessary in order to confirm and refine this scenario. Specifically, they are needed to accurately characterise the CEN and outflow physical properties and understand the role of the outflow in transporting metals in the CGM.

References

Allen, M. G., Groves, B. A., Dopita, M. A., Sutherland, R. S., & Kewley, L. J. 2008, ApJS, 178, 20

Arrigoni Battaia, F., Hennawi, J. F., Prochaska, J. X., & Cantalupo, S. 2015a, ApJ, 809, 163

Arrigoni Battaia, F., Yang, Y., Hennawi, J. F., et al. 2015b, ApJ, 804, 26

Arrigoni Battaia, F., Hennawi, J. F., Cantalupo, S., & Prochaska, J. X. 2016, ApJ, 829, 3

Arrigoni Battaia, F., Chen, C.-C., Fumagalli, M., et al. 2018, A&A, 620, A202

Arrigoni Battaia, F., Hennawi, J. F., Prochaska, J. X., et al. 2019, MNRAS, 482, 3162

Bacon, R., Accardo, M., Adjali, L., et al. 2010, in Ground-based and Airborne Instrumentation for Astronomy III, SPIE Conf. Ser., 7735, 773508

Bacon, R., Conseil, S., Mary, D., et al. 2017, A&A, 608, A1

Bischetti, M., Piconcelli, E., Vietri, G., et al. 2017, A&A, 598, A122

Bischetti, M., Piconcelli, E., Feruglio, C., et al. 2018, A&A, 617, A82

Borisova, E., Cantalupo, S., Lilly, S. J., et al. 2016, ApJ, 831, 39

Bruni, G., Piconcelli, E., Misawa, T., et al. 2019, A&A, 630, A111

Cai, Z., Fan, X., Bian, F., et al. 2017a, ApJ, 839, 131

Cai, Z., Fan, X., Yang, Y., et al. 2017b, ApJ, 837, 71

Cai, Z., Cantalupo, S., Prochaska, J. X., et al. 2019, ApJS, 245, 23

Cantalupo, S. 2017, in Gas Accretion onto Galaxies, eds. A. Fox, & R. Davé, Astrophys. Space Sci. Lib., 430, 195

Cantalupo, S., Porciani, C., Lilly, S. J., & Miniati, F. 2005, ApJ, 628, 61

Cantalupo, S., Arrigoni-Battaia, F., Prochaska, J. X., Hennawi, J. F., & Madau, P. 2014, Nature, 506, 63

Cantalupo, S., Pezzulli, G., Lilly, S. J., et al. 2019, MNRAS, 483, 5188

Christensen, L., Jahnke, K., Wisotzki, L., & Sánchez, S. F. 2006, A&A, 459, 717

Chung, A. S., Dijkstra, M., Ciardi, B., Kakiichi, K., & Naab, T. 2019, MNRAS, 484, 2420

Dijkstra, M., Haiman, Z., & Spaans, M. 2006, ApJ, 649, 37

Duras, F., Bongiorno, A., Piconcelli, E., et al. 2017, A&A, 604, A67

Farina, E. P., Arrigoni-Battaia, F., Costa, T., et al. 2019, ApJ, 887, 196

Faucher-Giguère, C.-A., & Quataert, E. 2012, MNRAS, 425, 605

Fiore, F., Feruglio, C., Shankar, F., et al. 2017, A&A, 601, A143

Ginolfi, M., Maiolino, R., Carniani, S., et al. 2018, MNRAS, 476, 2421

Gronke, M., & Dijkstra, M. 2016, ApJ, 826, 14

Heckman, T. M., Lehnert, M. D., Miley, G. K., & van Breugel, W. 1991, ApJ, 381, 373

Hennawi, J. F., & Prochaska, J. X. 2013, ApJ, 766, 58

Hennawi, J. F., Prochaska, J. X., Cantalupo, S., & Arrigoni-Battaia, F. 2015, Science, 348, 779

Hogan, C. J., & Weymann, R. J. 1987, MNRAS, 225, 1P

Humphrey, A. 2019, MNRAS, 486, 2102

Humphrey, A., Villar-Martín, M., Fosbury, R., Vernet, J., & di Serego Alighieri, S. 2006, MNRAS, 369, 1103

Humphrey, A., Villar-Martín, M., Fosbury, R., et al. 2007, MNRAS, 375, 705

Humphrey, A., Vernet, J., Villar-Martín, M., et al. 2013, ApJ, 768, L3

Laursen, P., Sommer-Larsen, J., & Andersen, A. C. 2009, ApJ, 704, 1640

Lusso, E., Worseck, G., Hennawi, J. F., et al. 2015, MNRAS, 449, 4204

Lusso, E., Fumagalli, M., Fossati, M., et al. 2019, MNRAS, 485, L62

Marino, R. A., Cantalupo, S., Pezzulli, G., et al. 2019, ApJ, 880, 47

Menci, N., Fiore, F., Feruglio, C., et al. 2019, ApJ, submitted [arXiv:1904.07621]

Møller, P., & Warren, S. J. 1998, MNRAS, 299, 661

Planck Collaboration VI. 2018, A&A, submitted [arXiv:1807.06209]

Shen, Y., Brandt, W. N., Richards, G. T., et al. 2016, ApJ, 831, 7

Silva, M., Humphrey, A., Lagos, P., et al. 2018, MNRAS, 474, 3649

Steidel, C. C., Erb, D. K., Shapley, A. E., et al. 2010, ApJ, 717, 289

Taniguchi, Y., & Shioya, Y. 2000, ApJ, 532, L13

van Ojik, R., Roettgering, H. J. A., Miley, G. K., & Hunstead, R. W. 1997, A&A, 317, 358

Verhamme, A., Schaerer, D., & Maselli, A. 2006, A&A, 460, 397

Vietri, G., Piconcelli, E., Bischetti, M., et al. 2018, A&A, 617, A81

Villar-Martín, M., Vernet, J., di Serego Alighieri, S., et al. 2003, in Rev. Mex. Astron. Astrofis. Conf. Ser., eds. V. Avila-Reese, C. Firmani, C. S. Frenk, & C. Allen, 17, 260

Villar-Martín, M., Sánchez, S. F., Peletier, R., et al. 2006, Astron. Nachr., 327, 187

Villar-Martín, M., Humphrey, A., De Breuck, C., et al. 2007a, MNRAS, 375, 1299

Villar-Martín, M., Sánchez, S. F., Humphrey, A., et al. 2007b, MNRAS, 378, 416

Weidinger, M., Møller, P., & Fynbo, J. P. U. 2004, Nature, 430, 999

Weidinger, M., Møller, P., Fynbo, J. P. U., & Thomsen, B. 2005, A&A, 436, 825

Weilbacher, P. M., Streicher, O., Urrutia, T., et al. 2014, in Astronomical Data Analysis Software and Systems XXIII, eds. N. Manset, & P. Forshay, ASP Conf. Ser., 485, 451

Wilman, R. J., Johnstone, R. M., & Crawford, C. S. 2000, MNRAS, 317, 9

Appendix A: Stellar contamination
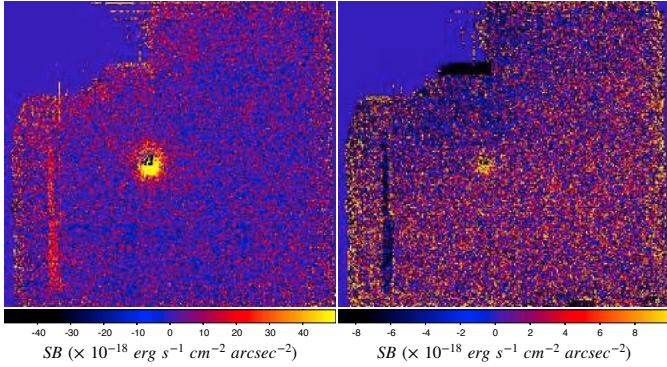
Fig. A.1. Images obtained by collapsing the final PSF- and continuum-subtracted datacubes in the spectral regions of Lyα- (*left panel*) and CIV-CEN (*right panel*), respectively. The homogeneous blue area on the upper-left corner represents the mask applied to the exposures during the data reduction in order to exclude the saturated stellar flux in the FOV.

Figure A.1 reports the image of the MUSE FOV that was obtained by collapsing the spectral region of the Lyα- (left) and CIV- (right) CEN in the PSF- and continuum-subtracted datacube. The upper-left corner of each image represents the region that is contaminated by the luminous star, which was masked during the data reduction. A visual inspection reveals no residual contamination at the CEN position. We performed a more quantitive estimation by measuring the average flux in concentric annular regions centred on the star. We found no significant stellar contamination on the nebular emissions. The average contamination was estimated in concentric annuli with respect to the centre of the star by excluding the nebular region. We estimated

a stellar contamination of the order of ~11%, ~6%, and ~6% in the north and south Lyα-CEN regions and over the entire CIV-CEN, respectively.

Appendix B: Blue tail

In this Appendix we report on several tests we performed in order to check for possible contamination of the weak CEN emission from the bright quasar emission line residuals after the Lyα subtraction. The left panel of Fig. B.1 shows the SB emission of the more blueshifted portion of the blue tail (i.e. highlighted in red in the right panel). This was obtained by collapsing the spectral region including the wing of the blue tail in order to avoid any possible contamination of the narrow Lyα component. To remove possible residuals at each pixel, we applied a subtraction of the continuum, which was measured from the spectral region highlighted in green in Fig. B.1. The final pseudo-NB image exhibits an asymmetric shape with respect to the quasar position and it is spatially associated with the peak of the SB of the Lyα-CEN. In case of residual AGN contribution, we would have expected a symmetric emission around the quasar. This provides an indication that the blue tail is not the result of emission line contamination from the quasar Lyα.

We find that the average intensity of the PSF subtraction residuals are three times lower than the intensity of the blue tail, which is, moreover, spatially coincident with a high S/N region. We further checked the quasar emission line contamination by inspecting the region of the bright quasar SiIV emission line. We measured the PSF-subtracted radial profile of the slope of the blue tail at the wavelength of the SiIV line. We found a flat radial profile with an average value around zero. This provides a further indication that the quasar emission does not contribute to the blue tail emission and, hence, that this is a genuine and intrinsic emission of the CEN.
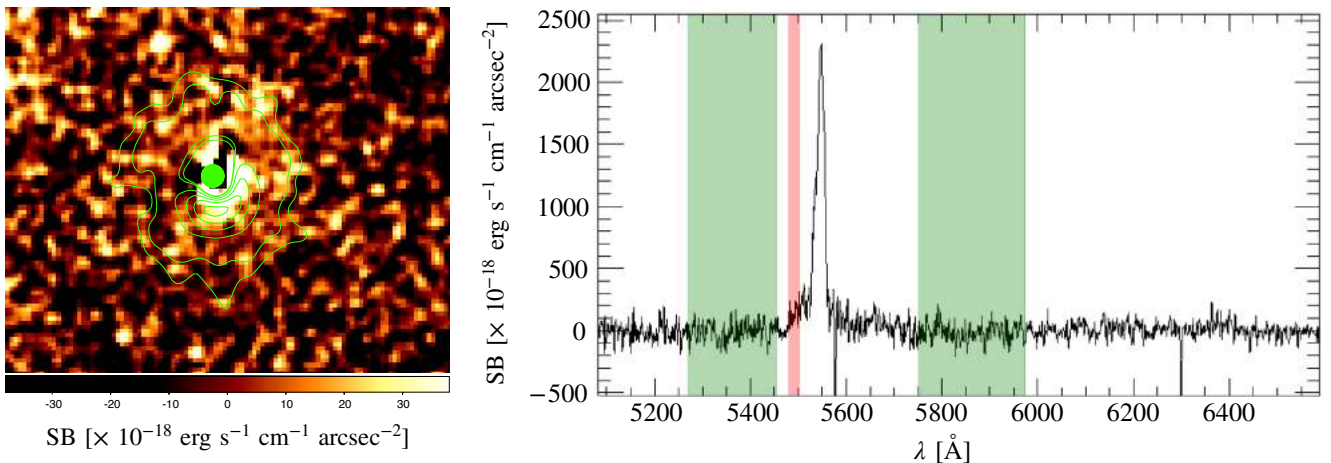
Fig. B.1. *Left panel*: pseudo-NB image obtained by collapsing the spectral region of the blue tail (see red area in the *right panel*) and by subtracting the continuum estimated in spectral regions without line features (see green areas in the *right panel*). *Right panel*: spectrum that is extracted from the PSF- and continuum-subtracted datacube by only selecting the spaxels that belong to the CEN with $S/N > 5$. The red and green areas mark the spectral region that is collapsed and subtracted, respectively, to obtain the pseudo-NB in the *left panel*.